

# Bioinspired High-Performance Energetic Materials Using Heme-Containing Crystals

Joseph M. Slocik, Lawrence F. Drummy, Matthew B. Dickerson,  
Christopher A. Crouse, Jonathan E. Spowart, and Rajesh R. Naik\*

Currently, there is a large demand for materials that offer new energy-efficient sources and participate in high-yield reactions. Unfortunately, energetic materials made up of traditional fuel-oxidizer mixtures have reached their limit of energetic performance. Engineering energetic nanocomposite materials composed of metallic fuels and inorganic oxidizers with nanoscale dimensions is an emerging field for reactive material systems. Of late, there has been growing interest in utilizing aluminum nanoparticles (nAl) as an energetic nanomaterial because of their intrinsically large surface area, high energy density, and excellent combustion/reaction kinetics.<sup>[1]</sup> However, identification of oxidizing agents represents a significant challenge to achieving maximum energy output from nAl. Ideally, the correct combination of oxidizer and nAl fuel should lead to the total release of its theoretical amount of energy ( $31 \text{ kJ g}^{-1}$ ).<sup>[2]</sup> In reality, the actual energy released is much less ( $\approx 15\%$  of the theoretical energy)<sup>[3–5]</sup> and highly depends on the choice of oxidizing material. The assembly, size, homogeneity, and interfacial interactions between the (metallic) fuel and the oxidizer (ferric oxide, ammonium perchlorate) influence the combustion/reaction kinetics of the energetic composites. Different approaches to increase the intimacy of the reactants to minimize the mass transport/diffusion of the components have been investigated. Recently, energetic nanocomposites have been assembled using bioenabled methods as an approach toward overcoming mass transport/diffusion limitations of traditional fuel-oxidizer mixtures by precisely controlling the assembly of energetic components.<sup>[6,7]</sup> For example, protein cages loaded with iron oxide nanoparticles or ammonium perchlorate oxidizing agents were directly assembled onto the surface of nAl to create a biothermite energetic nanocomposite.<sup>[6]</sup> These bioassembled nanocomposite mate-

rials attained enhanced reaction rates and increased energetic properties when compared to heterogeneous mixtures, whereas the use of traditional oxidizing materials limited the stability and amount of energy released from nAl. Empirically, the exploration of oxidizing materials has been so far restricted to a handful of nanometer-sized metal oxides (CuO, Fe<sub>3</sub>O<sub>4</sub>, FeO(OH), MnO),<sup>[4,8]</sup> chemical oxidizing agents (NH<sub>4</sub>ClO<sub>4</sub>, H<sub>2</sub>O<sub>2</sub>, NH<sub>4</sub>NO<sub>3</sub>, and water),<sup>[9]</sup> and in a few cases fluorinated polymers.<sup>[10–12]</sup> In total, some of these materials are hazardous, unstable, and conventionally outdated.

Nature offers an abundant source of bio-oxidation reactions that employ energetic components with unique structures, properties, and activities that can rival man-made materials.<sup>[13]</sup> These include biologically produced inorganic nanomaterials,<sup>[13,14]</sup> redox active enzymes,<sup>[15]</sup> and an assortment of molecular oxidizing agents.<sup>[16,17]</sup> Advantages of bio-oxidation materials are its low cost, excellent stability, high activity, and ease of handling. Of these materials, iron porphyrins act as strong oxidizing agents in nature and are critical to the function of many different biological systems.<sup>[18]</sup> Compositionally, they represent the basic heme subunit that imparts oxygenation activity to hemoglobin and myoglobin,<sup>[19]</sup> and form the active sites in peroxidase and catalase enzymes.<sup>[20]</sup> The malaria parasite, *Plasmodium falciparum*, produces hemozoin crystals—a highly reactive inorganic biomineral—from heme, during the intraerythrocytic growth cycle of the parasite.<sup>[21]</sup> In its microcrystalline form, hemozoin is nontoxic and insoluble to the parasite, but highly reactive and symptomatic to the host.<sup>[22]</sup> Physiologically, hemozoin crystal deposits are the primary cause of malaria's clinical symptoms (inflammation, fever, anemia, skin/organ discoloration) due to hemozoin-catalyzed oxidation reactions in vivo (lipid oxidation, peroxidase activity).<sup>[23,24]</sup> Unlike many other biologically produced materials, hemozoin is a byproduct of no known commercial value. However, hemozoin can be a viable component for energetic materials due to the presence of iron(III)-oxygen groups ( $\approx 10^7$  heme molecules) that are well suited for the oxidation of inorganic materials.<sup>[25,26]</sup> In this study, we utilized this atypical biologically inspired source of oxidizing material to increase the energetic output and performance of nAl, while maintaining energetic performance through geometrical optimization of the nanostructure assembly. Energetically, the hemozoin acted as a strong molecular oxidizing agent/thermite material to rapidly oxidize the nAl fuel, releasing large amounts of energy.

Dr. J. M. Slocik, Dr. L. F. Drummy, Dr. M. B. Dickerson,  
Dr. J. E. Spowart, Dr. R. R. Naik  
Materials and Manufacturing Directorate  
Air Force Research Laboratory  
Wright-Patterson AFB, OH 45433, USA  
E-mail: rajesh.naik@us.af.mil



Dr. C. A. Crouse  
Munitions Directorate  
Air Force Research Laboratory  
Eglin AFB, FL 32542, USA  
DOI: 10.1002/sml.201403659

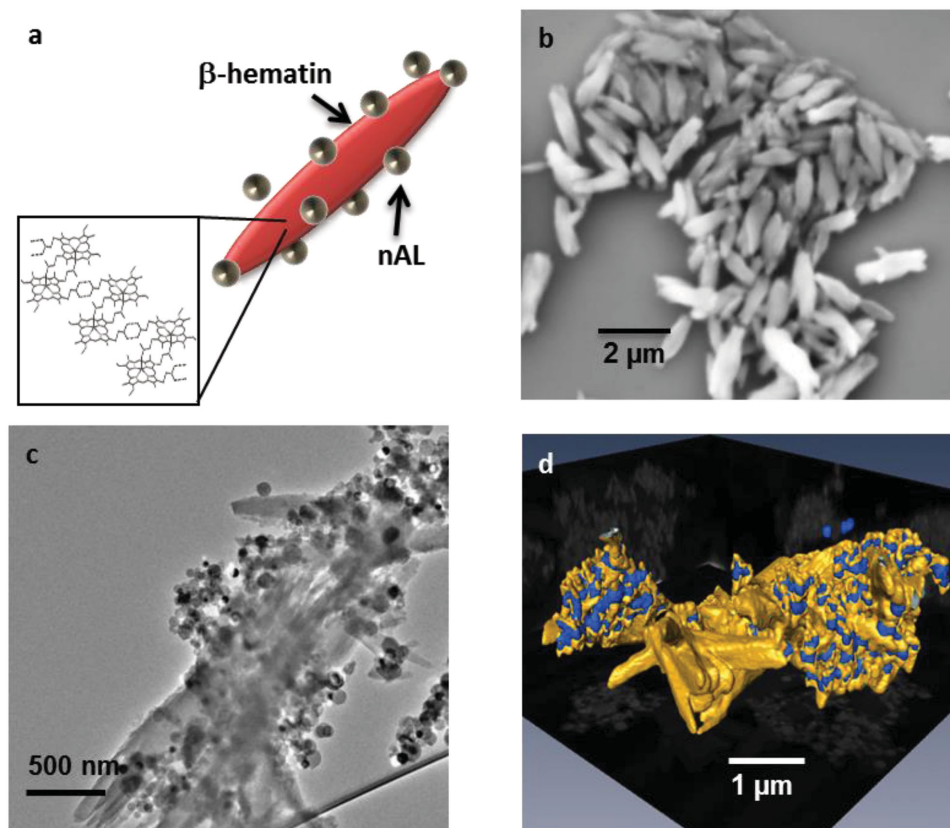


**Figure 1.** Assembly and characterization of nAl with  $\beta$ -hematin crystals composites. a) Schematic illustration of nAl–protamine at 40 wt% nAl decorated onto  $\beta$ -hematin crystals ( $\phi = 17.7$ ). b) SEM micrograph of synthetic needle-like  $\beta$ -hematin crystals. c) TEM micrograph of nAl–protamine– $\beta$ -hematin composites. d) Reconstructed electron tomography image of nAl (in blue): $\beta$ -hematin (in gold) composite materials. Slices of the structure are depicted by bright field TEM images through  $x$ ,  $y$ , and  $z$  planes.

To obtain a source of hemozoin, we chose to use the synthetic form of hemozoin ( $\beta$ -hematin) instead of isolating it from parasite-infected red blood cells.  $\beta$ -hematin is a well-known synthetic analog of hemozoin that is chemically, spectroscopically, and crystallographically identical.<sup>[27]</sup> Also, it can be produced at a low cost and in large quantities using a simple synthetic method.<sup>[28]</sup> Structurally, hemozoin and  $\beta$ -hematin crystals are composed of iron porphyrin dimers polymerized through iron (III)–oxygen bonds and assembled through  $\pi$ – $\pi$  stacking of the porphyrin rings that result in long thin needle-like morphologies with high aspect ratios (Figure 1b).<sup>[25]</sup> Following a previously established protocol, we synthesized  $\beta$ -hematin from the polymerization of hemin.<sup>[28]</sup> Morphological characterization using TEM and SEM showed the presence of needle-like crystals consistent with native hemozoin and synthetic  $\beta$ -hematin (Figure 1a–d).<sup>[29]</sup> Structural characterization using X-ray diffraction (XRD) of the  $\beta$ -hematin crystals was indexed to the known diffraction pattern of hemozoin (see Figure S1, Supporting Information).<sup>[30]</sup>

For the assembly of the energetic nanomaterial, nAl was electrostatically assembled onto  $\beta$ -hematin using protamine to minimize the diffusion distance/mass transport between the fuel and the oxidizer. Protamine is a positively charged polypeptide (zeta potential  $\zeta = +17.2 \pm 0.3$  mV) and has been used as a self-assembly directing reagent for metal oxide

nanoparticles.<sup>[31,32]</sup> Also, we used protamine for its ability to passivate the surface of nAl and increase its stability under mild biological oxidizing conditions (water, 40 °C) and improve its shelf-life. For example, nAl functionalized with protamine was significantly more resistant to oxidation in water at 40 °C versus bare unfunctionalized nAl that oxidized rapidly to  $\text{Al}(\text{OH})_3$  under the same conditions (>27 vs 1 d) (see Figure S2, Supporting Information). Consequently, nAl was functionalized with protamine and then assembled onto  $\beta$ -hematin crystals to yield 60 wt%  $\beta$ -hematin and an equivalency ratio of 17.7 [equivalency ratio  $\phi = (\text{fuel}/\text{oxidizer})_{\text{actual}}/(\text{fuel}/\text{oxidizer})_{\text{stoichiometric}}$ ]. By transmission electron microscopy (TEM), the crystals were coated with aggregates of multiple nAl particles along the crystal surface (Figure 1c). In the absence of protamine, there were substantially fewer nAl particles associated with the  $\beta$ -hematin crystals (see Figure S3, Supporting Information). Geometrically, the needle-like morphology allowed the assembly of a large number of spherical nAl particles as depicted by the reconstructed structure from electron tomography (Figure 1d). This configuration precluded the need to assemble multiple layers of ferritin to meet stoichiometric conditions, as required in our previous bio-based thermite material.<sup>[6]</sup>

Upon assembly, the energy output and performance of our bio-inspired nanoenergetic composite materials were characterized by simultaneous differential thermal analysis/thermal

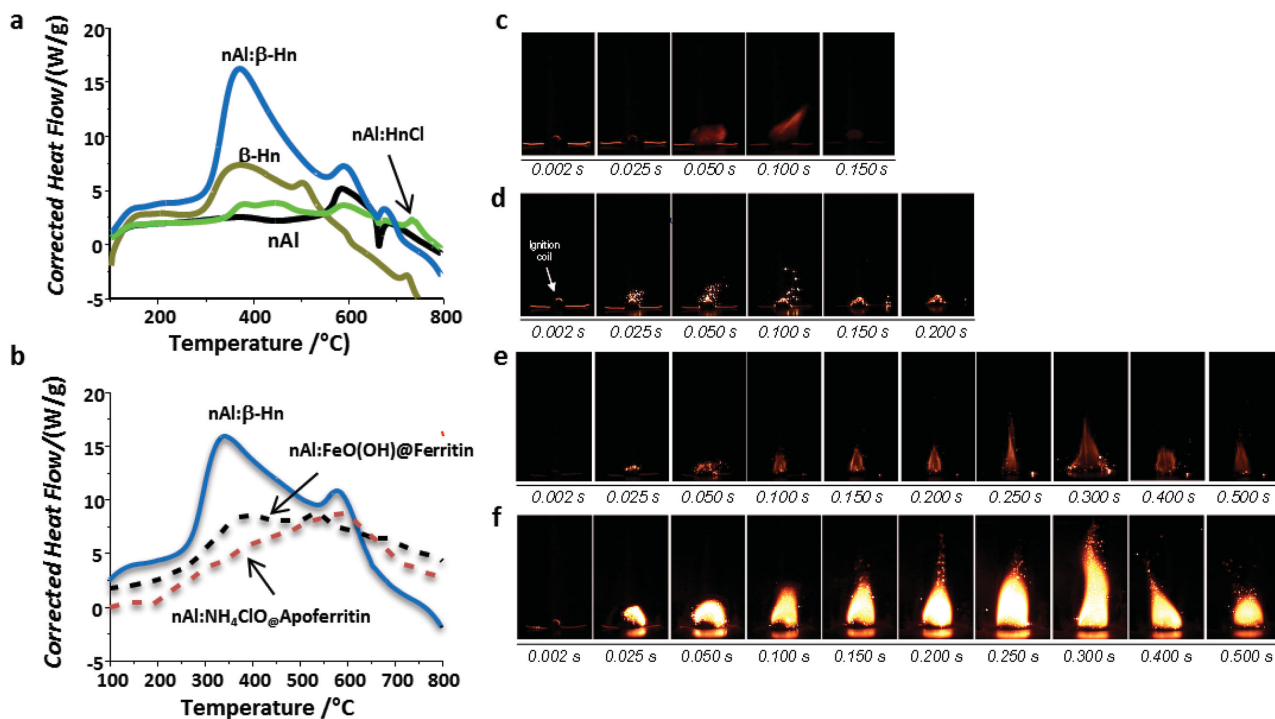


**Figure 2.** Characterization of energetic properties. a) Differential thermal analysis profile (DTA) displaying the heat flow of nAl- $\beta$ -hematin composite at 60 wt%  $\beta$ -hematin ( $\phi = 17.7$ ), free  $\beta$ -hematin (b-Hn), nAl-hemin (nAl:HnCl) at 70 wt% hemin ( $\phi = 10.7$ ), and unassembled nAl using a TA instruments SDT Q600 DTA/TGA instrument. Energy density was obtained by dividing the raw heat flow from DTA by the original sample weight. Heat flow was measured under Ar gas at 100 mL  $\text{min}^{-1}$  flow rate and at a temperature ramp of 20  $^{\circ}\text{C min}^{-1}$ . b) DTA profile of nAl: $\beta$ -hematin composite, nAl-ferritin containing FeO(OH), and nAl-apoferritin containing  $\text{NH}_4\text{ClO}_4$ . High-speed digital color video time frame snapshots showing the reaction of 15 mg of material in a vented combustion chamber using a resistively heated copper coiled wire to initiate reaction of c) pure  $\beta$ -hematin only, d) nAl particles functionalized with protamine, e) nAl-protamine assembled with hemin (70 wt%), and f) nAl-protamine assembled with  $\beta$ -hematin (60 wt%).

gravimetric analysis (DTA/TGA) from 25 to 800  $^{\circ}\text{C}$  in a 100% argon environment to prevent air oxidation. DTA analysis is routinely used to characterize energetic materials and provides details about exothermic events and total amount of energy released from materials. As a benchmark, the DTA profile of unassembled nAl showed a sharp endothermic peak at  $\approx 660$   $^{\circ}\text{C}$  due to aluminum melting and a broad exotherm, which also corresponds to the weight gain observed by TGA, likely due to very minor oxidation from some external oxygen source (see Figure S4, Supporting Information) (Figure 2a, black line).<sup>[33]</sup> This characteristic melting peak provides a means to assess the energetic reaction by determining how much aluminum is consumed and whether stoichiometric conditions are reached. We next examined the heat released from unassembled  $\beta$ -hematin ( $\beta$ -Hn) crystals to determine their energetic content (Figure 2a, olive green line). Similarly, the DTA heat flow profile revealed a small broad exotherm at 350  $^{\circ}\text{C}$ , a large endothermic decay response that started at  $\approx 550$   $^{\circ}\text{C}$ , and a heat of combustion of +3.4  $\text{kJ g}^{-1}$ . The small exothermic peak was likely due to internal oxidation of iron and the porphyrin ring and was consistent with the DSC of proteins and biomass in inert atmospheres,<sup>[34,35]</sup> whereas the large endothermic region coincided with a 60% weight loss by TGA (see Figure S4, Supporting Information) that proceeds via decomposition/volatilization.

Using a color high-speed digital video, we recorded the ignition of each material in an open air-vented fragmentation

chamber. The set of combustion images (Figure 2c,d) shows that nAl and  $\beta$ -hematin individually exhibited minimal combustion, as expected. Ignition of  $\beta$ -hematin showed a slow (candle-like) burning characteristic of organic matter, whereas nAl reacted slowly based on limited diffusion of atmospheric oxygen. In both controls, we lacked the complementary fuel and the oxidizer, respectively. In addition, we considered the combustion of nAl-protamine assembled with 70 wt% hemin (nAl:HnCl,  $\phi = 10.7$ , molecular precursor to  $\beta$ -hematin) (Figure 2e). When assembled, this precursor material resulted in a weak energetic event by DTA (+4.3  $\text{kJ g}^{-1}$ , Figure 2a, green line) and generated only a slightly greater flame than nAl or  $\beta$ -hematin by a high-speed video. In this case, the lack of a substantial exotherm and combustion event for nAl-hemin is consistent with the DTA plot and performance of nAl/ammonium perchlorate materials and represents the thermal decomposition of free  $\text{NH}_4\text{ClO}_4$  and hemin before reaction with nAl.<sup>[6,36]</sup>

For nAl assembled with  $\beta$ -hematin (nAl: $\beta$ -Hn), the DTA plot revealed a large broad exotherm with an onset temperature at 100  $^{\circ}\text{C}$ , multiple exothermic peaks, loss of the aluminum melting peak, and a heat of combustion of  $+12.5 \pm 2.4$   $\text{kJ g}^{-1}$  (Figure 2a, blue line, see Figure S5, Supporting Information). The experimentally determined heat of combustion value is in approximate agreement with the theoretically predicted energy density of +10.3  $\text{kJ g}^{-1}$  calculated from the respective enthalpies of formation (see Figure S5, Supporting

information). The pair of exothermic peaks generated at  $\approx 340$  and  $580$  °C corresponds to those from a thermite-type reaction and oxidation by a molecular oxidizing agent, respectively (Figure 2b).<sup>[37]</sup> With the nAl: $\beta$ -Hn nanocomposite materials, the larger exotherm at  $340$  °C indicates that the thermite reaction is the dominant mechanism of heat release. Notably, unassembled nAl powder mixed with 60 wt%  $\beta$ -hematin exhibited much lower heat flows and also incomplete oxidation, as shown by small melting endotherm around  $660$  °C (see Figure S6, Supporting Information). Using high-speed digital video, ignition of nAl: $\beta$ -Hn nanocomposite showed excellent reaction/combustion characteristics that included fast initiation ( $\approx 25$  ms), generation of an intense hot flame based on luminosity, sustained reaction up to 1 s, and complete deflagration as shown in Figure 2f. The difference in performance between free hemin and  $\beta$ -hematin with nAl is large and due to the increased decomposition of hemin and/or the presence of Cl as confirmed above. Energetically, the geometrical configuration of nAl: $\beta$ -Hn promotes the generation of a self-propagating reaction wave front along the length of the oxidizer crystal and contributes to greater energy release even though this a heterogeneous mixture.<sup>[38]</sup> nAl: $\beta$ -Hn nanocomposite produced a similar heat flow profile to both nAl(FeO(OH)@ferritin) and nAl(NH<sub>4</sub>ClO<sub>4</sub>@apoferritin) composite materials but released much more heat over the same temperature

region (Figure 2b). These similarities in exothermic behavior to nAl with FeO(OH) or NH<sub>4</sub>ClO<sub>4</sub> are likely due to the abundance of iron–oxygen covalent bonds present in  $\beta$ -hematin, as well as open coordination sites on Fe<sup>3+</sup> of heme.

To provide insight into the oxidation reaction and the identity of the resulting products, we examined nAl: $\beta$ -Hn nanocomposites before and after burning by Fourier transform infrared spectroscopy (FT-IR), X-ray photoelectron spectroscopy (XPS), powder X-ray diffraction (XRD), and TEM. After burning, the FT-IR spectrum showed the loss of almost all stretching vibrations associated with the porphyrin rings of  $\beta$ -hematin (see Figure S7, Supporting Information), whereas XPS showed the complete loss of the N1s signal and a significant decrease in the C1s peak (see Figure S8, Supporting Information). This is consistent with the loss of structural and chemical integrity of the  $\beta$ -hematin porphyrin rings, release of nitrogen gas, conversion of carbon during the high-temperature oxidation process, and loss of mass by TGA analysis (see Figure S4, Supporting Information). The identity of this material was confirmed by XRD to be mostly amorphous soot-like material with major products assigned to Al<sub>2</sub>O<sub>3</sub> and maghemite Fe<sub>2</sub>O<sub>3</sub> (see Figure S9, Supporting Information).<sup>[39]</sup> Maghemite is superparamagnetic at room temperature and we were able to demonstrate a collection of the soot material using an external magnet (Figure 3a).

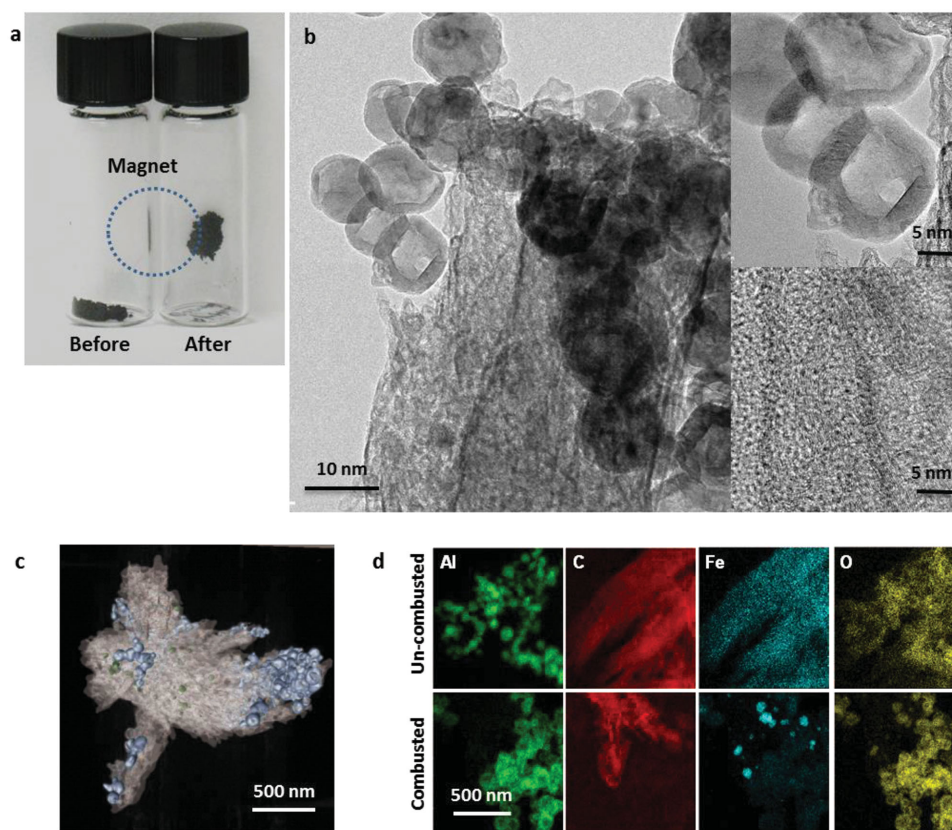


**Figure 3.** Reaction products of nAl( $\beta$ -hematin). a) Effects of external magnet on nAl: $\beta$ -hematin composite powder before and after DTA analysis. b) HRTEM images of nAl: $\beta$ -hematin composites after DTA depicting empty alumina shells and carbon products. Higher magnification images of alumina shells (upper right) and graphitic carbon (lower right). c) Reconstructed electron tomography image of nAl( $\beta$ -hematin) materials after DTA (top down view). In the 3D reconstructed image,  $\beta$ -hematin crystals are tan, Al<sub>2</sub>O<sub>3</sub> particles are blue, and Fe<sub>2</sub>O<sub>3</sub> deposits are green. Slices of the structure are depicted by bright field TEM images through x, y, and z planes. d) EDS maps of Al, C, Fe, and O of unreacted nAl( $\beta$ -hematin) (top row) and nAl( $\beta$ -hematin) after burning (bottom row).

Minor products included peaks associated with unreacted nAl due to an incomplete reaction and inefficient burning. Morphologically, TEM revealed that  $\beta$ -hematin became more porous in nature and consisted of graphitic carbon nanofibers ( $d$ -spacing 3.4 Å) with small embedded  $\text{Fe}_2\text{O}_3$  particles, but retained its overall needle-like structure and crystal dimensions (Figure 3b, see Figure S10, Supporting Information). The nAl particles appeared as empty shells of alumina due to a diffusion-based mechanism and consumption of the aluminum metal core upon reaction with  $\beta$ -hematin (Figure 3b).<sup>[40–43]</sup> Notably, the creation of graphitic carbon nanofibers from  $\beta$ -hematin is favored under the conditions (high temperatures, pressures, and presence of Fe catalyst) generated during the combustion of the organic material.<sup>[44]</sup> This altered morphology was evident in the 3D reconstructed electron tomography image of the combustion material and observed to be alumina, iron oxide, and carbon-rich materials based on X-ray energy dispersive spectroscopy (EDS) maps (Figure 3c,d). In total, these products were equivalent to those expected from a thermite reaction.

In this study, we demonstrate that biologically inspired materials represent a new class of energetic materials exploiting the functionality and control of biology and providing an inexpensive source of reactive components.  $\beta$ -hematin crystals assembled with nAl can create a high-performance energetic nanocomposite. The  $\beta$ -hematin provided a highly reactive crystal surface for the oxidation of nAl and led to rapid energy release. These materials were more reactive and released more energy than nAl assembled with ammonium perchlorate,<sup>[45]</sup> periodate salts,<sup>[46]</sup> graphene oxide,<sup>[5]</sup>  $\text{MoO}_3$ ,<sup>[47]</sup> fluorinated polymers,<sup>[10]</sup> or  $\text{CuO}$ .<sup>[7]</sup> Although hemozoin is a strong oxidant by itself, the introduction of an additional oxidizing source (inorganic nanoparticles and/or molecular oxidizing agents) could complement hemozoin and provide even greater energetics. In addition, the crystalline maghemite products created from nAl: $\beta$ -hematin composite combustion can serve as a new source for a second combustion reaction with additional nAl. The development of a high-performance nAl: $\beta$ -hematin nanoenergetic composite using bioinspired materials represents a major step toward the development of safer, low-cost multifunctional materials for combustion systems. Interestingly, from the nAl: $\beta$ -hematin combustion process, conversion of hemozoin waste products into bundles of graphitic nanofibers could lead to a synthetic route for high-quality graphitic fibers for wide-ranging applications.

## Experimental Section

**Assembly of nAl:( $\beta$ -Hematin) Composites:** Aluminum nanoparticles (80 nm, 80% active Al content) passivated with an amorphous aluminum oxide were obtained from Novacentrix, Inc. 10 mg of aluminum nanoparticle powder was suspended in 5 mL of deionized water and sonicated using an ultrasonic bath for 5 min to disperse nAl particles. 2 mg of protamine (Sigma) was added to nAl suspension and incubated for 30 min. The nAl–protamine suspension was centrifuged at 14 000 rpm for 5 min, washed with water, and centrifuged again. This was repeated two more times to remove

excess unbound protamine. To obtain synthetic  $\beta$ -hematin crystals, we followed a slightly modified published protocol. Briefly, 15 mg of hemin chloride (Sigma-Aldrich) was dissolved in 3 mL of NaOH and combined with 1.74 mL of 12.8 m acetate buffer/0.3 mL 1 M HCl. The solution was incubated at 75 °C for 3 d in a vacuum oven. After 3 d, the  $\beta$ -hematin crystals were centrifuged at 11 000 rpm for 10 min, washed with 0.1 M sodium bicarbonate buffer pH 9.5, and again centrifuged at 11 000 rpm for 10 min. This washing procedure was repeated four times to remove uncrystallized free hemin-Cl. After four washes with the 0.1 M sodium bicarbonate buffer, the  $\beta$ -hematin was washed with deionized water, centrifuged three more times, and lyophilized. Approximately 10 mg of nAl–protamine was assembled with  $\approx$ 10 mg of  $\beta$ -hematin in 1 mL of deionized water, sonicated for 5 min, incubated for 30 min, and frozen and lyophilized to obtain an assembled structure.

**Characterization:** FT-IR was performed on a Bruker Alpha FT-IR spectrometer using a universal sampling module. nAl: $\beta$ -hematin samples were prepared as a KBr pellet and spectra were collected and averaged over 20 scans and blanked against air. SEM images were obtained on a FEI Quanta eSEM microscope operating at 10 kV and a working distance of 25 mm. Samples were spotted on a Si wafer and mounted on a standard SEM puck. Bright field TEM images were obtained on a Phillips CM200 transmission electron microscope operating at 200 kV. Samples were prepared by pipetting 10  $\mu\text{L}$  of nAl: $\beta$ -hematin onto a 3 mm 200 mesh copper TEM grid coated with ultrathin carbon film (Ted Pella) and air dried. For HRTEM images, electron tomography, and XEDS maps, an FEI  $\text{C}_s$ -corrected Titan TEM microscope operating at 300 kV was used. To collect electron tomography, we used scanning transmission electron microscopy (STEM) mode with spot size 6, gun lens 1, and a convergence angle of 9.6 mrad. Images were collected using a Fischione high-angle annular dark field (HAADF) detector at a camera length of 105 mm, with an inner detector angle of 60 mrad, and an outer detector angle of 300 mrad. Tilt series were collected over a range of  $-65^\circ$  to  $+65^\circ$ , with a  $2^\circ$  tilt increment. Cross correlation alignment was performed to subpixel accuracy after acquisition. Model Based Iterative Reconstruction (MBIR, www.OpenMBIR.org) was used for the reconstruction of the aligned data. X-ray energy dispersive spectroscopy (XEDS) was done in STEM mode with a sample tilt of  $15^\circ$  and an EDAX detector. XPS measurements were performed using an M-PROBE Surface Science XPS spectrometer utilizing charge neutralization. Samples were prepared by drop-casting 10  $\mu\text{L}$  of an aqueous suspension of nAl: $\beta$ -hematin onto a polished silicon wafer (Wafer world) before and after combustion and air dried. Spectra were collected from 0 to 1000 eV at 1 eV steps at a spot size of 800  $\mu\text{m}$  and averaged over 25 scans. High-resolution scans were collected at 0.01 eV steps and averaged over 100 scans. X-ray diffraction (XRD) analyses were conducted with a Bruker D2 phaser diffractometer equipped with a Lynxeye Si strip detector and utilized  $\text{Cu K}\alpha$  radiation. Approximately 5 mg of powder from each sample was placed on a zero background offset Si holder. Diffraction experiments used a scan rate of  $0.08^\circ \text{min}^{-1}$ . Phase analyses were conducted utilizing EVA (Bruker AXS, Madison, WI) and/or Jade (Materials Data Inc., Livermore, CA) software packages and a PDF database from the International Centre for Diffraction Data (Newtown Square, PA).

**Energetic Characterization:** Simultaneous thermogravimetric analysis (TGA) and differential thermal analysis (DTA) measurements were performed in a TA Instruments SDT Q 600. Samples ( $\approx$ 5 mg)

were placed into a tared alumina crucible with an empty alumina crucible serving as the reference. All data were collected in dynamic mode under flowing argon (100 mL min<sup>-1</sup>) from room temperature up to 800 °C at a rate of 20 °C min<sup>-1</sup>. Heats of combustion in kJ g<sup>-1</sup> were obtained by measuring the area of the DTA peaks plotted versus time (s) from 25 to 800 °C. Combustion experiments were performed by placing approximately 10 mg of the respective  $\beta$ -hematin, nAl, or assembled nAl: $\beta$ -hematin powder onto a flat steel gauze substrate in a vented fragmentation chamber under an air atmosphere. The powders were initiated by a heated coil directly contacting the sample. A NAC Image Technology Memrecam GX8 digital high-speed video camera, collecting full frame, full color images at 5000 frames per second, was used to record the combustion event.

## Supporting Information

Supporting Information is available from the Wiley Online Library or from the author.

## Acknowledgements

This work was funded by the Air Force Office Scientific Research. The authors thank Dr. Alexander Khramov (UES, Inc.) for assistance with high-speed video images of combustion events and Mr. Nicholas Garvin for technical assistance with reconstructing electron tomography data.

- [1] E. L. Dreizin, *Prog. Energy Combust. Sci.* **2009**, *35*, 141.
- [2] C. E. Holley, Jr., E. J. Huber Jr, *J. Am. Chem. Soc.* **1951**, *73*, 5577.
- [3] A. Shahnavan, T. Desai, T. Matsoukas, *ACS Appl. Mater. Inter.* **2014**, *6*, 7942.
- [4] V. K. Patel, S. Bhattacharya, *ACS Appl. Mater. Inter.* **2013**, *5*, 13364.
- [5] R. Thiruvengadathan, S. W. Chung, S. Basuray, B. Balasubramanian, C. S. Staley, K. Gangopadhyay, S. A. Ganaopadhyay, *Langmuir* **2014**, *30*, 6556.
- [6] J. M. Slocik, C. A. Crouse, J. E. Spowart, R. R. Naik, *Nano Lett.* **2013**, *13*, 2535.
- [7] F. Severac, P. Alphonse, A. Esteve, A. Bancaud, C. Rossi, *Adv. Funct. Mater.* **2012**, *22*, 323.
- [8] D. A. Kaplowitz, G. Q. Jian, K. Gaskell, R. Jacob, M. R. Zachariah, *J. Energ. Mater.* **2014**, *32*, 94.
- [9] G. A. Risha, T. L. Connell, R. A. Yetter, D. S. Sundaram, V. Yang, *Combust. Propul. Power* **2014**, *30*, 133.
- [10] C. A. Crouse, C. J. Pierce, J. E. Spowart, *Combust. Flame* **2012**, *159*, 3199.
- [11] X. Zhou, M. Torabi, J. Lu, R. Q. Shen, K. L. Zhang, *ACS Appl. Mater. Inter.* **2014**, *6*, 3058.
- [12] X. Zhou, D. Xu, G. Yang, Q. Zhang, J. Shen, J. Lu, K. Zhang, *ACS Appl. Mater. Inter.* **2014**, *6*, 10497.
- [13] M. B. Dickerson, K. H. Sandhage, R. R. Naik, *Chem. Rev.* **2008**, *108*, 4935.
- [14] D. A. Bazylinski, R. B. Frankel, K. O. Konhauser, *Geomicrobiol. J.* **2007**, *24*, 456.
- [15] S. G. Burton, *Trends Biotechnol.* **2003**, *21*, 543.
- [16] A. C. McIntosh, M. Forman, in *Design and Nature II*, WIT, Rhodes, Greece **2004**.
- [17] B. Halliwell, *Plant Physiol.* **2006**, *141*, 312.
- [18] K. D. Bewley, K. E. Ellis, M. A. Firer-Sherwood, S. J. Elliot, *Biochim. Biophys. Acta* **2013**, *1827*, 938.
- [19] R. D. Jones, D. A. Summerville, F. Basolo, *Chem. Rev.* **1979**, *79*, 139.
- [20] T. L. Poulos, *Chem. Rev.* **2014**, *114*, 3919.
- [21] D. J. Sullivan Jr., I. Y. Gluzman, D. E. Goldberg, *Science* **1996**, *271*, 219.
- [22] T. J. Egan, *J. Inorg. Biochem.* **2002**, *91*, 19.
- [23] N. Klonis, R. Dilanian, E. Hanssen, C. Darmanin, V. Streltsov, S. Deed, H. Quiney, L. Tilley, *Biochemistry* **2010**, *49*, 6804.
- [24] C. M. Miller, C. K. Carney, A. C. Schrimpe, D. W. Wright, *Inorg. Chem.* **2005**, *44*, 2134.
- [25] J. M. Pisciotto, D. Sullivan, *Parasitol. Int.* **2008**, *57*, 89.
- [26] G. P. Kotchey, B. L. Allen, H. Vedala, N. Yanamala, A. A. Kapralov, Y. Y. Tyurina, J. Klein-Seetharaman, V. E. Kagan, A. Star, *ACS Nano* **2011**, *5*, 2098.
- [27] S. Pagola, P. W. Stephens, D. S. Bohle, A. D. Kosar, S. K. Madsen, *Nature* **2000**, *404*, 307.
- [28] K. A. Cole, J. Ziegler, C. A. Evans, D. W. Wright, *J. Inorg. Biochem.* **2000**, *78*, 109.
- [29] M. Olivier, K. Van Den Ham, M. T. Shio, F. A. Kassa, S. Fougeray, *Front Immunol.* **2014**, *5*, 1.
- [30] S. Kapishnikov, T. Berthing, L. Hviid, M. Dierolf, A. Menzel, F. Pfeiffer, J. Als-Nielsen, L. Leiserowitz, *Proc. Natl. Acad. Sci. U. S. A* **2012**, *109*, 11184.
- [31] M. B. Dickerson, W. J. Lyon, W. E. Gruner, P. A. Mirau, M. L. Jespersen, Y. N. Fang, K. H. Sandhage, R. R. Naik, *Adv. Funct. Mater.* **2013**, *23*, 4236.
- [32] K. Radhakrishnan, S. Gupta, D. P. Gnanadhas, P. C. Ramamurthy, D. Chakravorty, A. M. Raichur, *Particle Particle Syst. Charact.* **2014**, *31*, 449.
- [33] *CRC Handbook of Chemistry and Physics*, 84th ed., CRC Press, Boca Raton, FL **2003**.
- [34] A. Cucos, P. Budrugaec, *J. Therm. Anal. Calorim.* **2004**, *115*, 2079.
- [35] D. Lopez-Gonzalez, M. Fernandez-Lopez, J. L. Valverde, L. Sanchez-Silva, *Appl. Energy* **2014**, *114*, 227.
- [36] S. F. Li, Z. Jiang, F. Q. Zhao, Z. R. Liu, C. M. Yin, Y. Luo, S. W. Li, *Chin. J. Chem. Phys.* **2004**, *17*, 623.
- [37] J. Wang, A. M. Hu, J. Persic, J. Z. Wen, Y. N. Zhou, *J. Phys. Chem. Solids* **2011**, *72*, 620.
- [38] C. Mandilas, G. Karagiannakis, A. G. Konstandopoulos, C. Beatrice, M. Lazzaro, G. Di Blasio, S. Molina, J. V. Pastor, A. Gil, *Energy Fuel* **2014**, *28*, 3430.
- [39] R. L. Vander Wal, A. J. Tomasek, *Combust. Flame* **2004**, *136*, 129.
- [40] K. W. Watson, M. L. Pantoya, V. I. Levitas, *Combust. Flame* **2008**, *155*, 619.
- [41] K. T. Sullivan, W.-A. Chiou, R. Fiore, M. R. Zachariah, *Appl. Phys. Lett.* **2010**, *97*, 133104.
- [42] G. C. Egan, K. T. Sullivan, T. LaGrange, B. W. Reed, M. R. Zachariah, *J. Appl. Phys.* **2014**, *115*, 084903.
- [43] K. T. Sullivan, N. W. Piekielek, C. Wu, S. Chowdhury, S. T. Kelly, T. C. Hufnagel, K. Fezzaa, M. R. Zachariah, *Combust. Flame* **2012**, *159*, 2.
- [44] J. Libera, Y. Gogotsi, *Carbon* **2001**, *339*, 1307.
- [45] S. Liu, M. Ye, A. Han, X. Chen, *Appl. Surf. Sci.* **2014**, *288*, 349.
- [46] G. Q. Jian, J. Feng, R. J. Jacob, G. C. Egan, M. R. Zachariah, *Angew. Chem., Int. Ed.* **2013**, *52*, 9743.
- [47] K. S. Kappagantula, C. Farley, M. L. Pantoya, J. Horn, *J. Phys. Chem. C* **2012**, *116*, 24469.

Received: December 9, 2014  
 Revised: March 12, 2015  
 Published online: May 5, 2015